







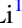

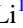

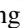

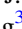
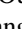
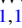




Broadband Variability Study of Maxī J1631-479 in Its Hard-intermediate State Observed with Insight-HXMT

Q. C. Bu^{1,2} , S. N. Zhang^{1,3} , A. Santangelo², T. M. Belloni⁴, L. Zhang⁵ , J. L. Qu^{1,3} , L. Tao¹ , Y. Huang^{1,3}, X. Ma¹, Z. S. Li⁶, S. Zhang¹, L. Chen⁷

and the Insight-HMXT collaboration;

C. Cai^{1,3}, X. L. Cao¹, Z. Chang¹, T. X. Chen¹, Y. Chen¹, Y. P. Chen¹, W. W. Cui¹, Y. Y. Du¹, G. H. Gao^{1,3} , H. Gao^{1,3} , M. Y. Ge¹ , Y. D. Gu¹, J. Guan¹, C. C. Guo^{1,3}, D. W. Han¹, J. Huo¹, S. M. Jia¹ , W. C. Jiang¹, J. Jin¹, L. D. Kong^{1,3} , B. Li¹ , C. K. Li¹ , G. Li¹, T. P. Li^{1,3,8}, W. Li¹, X. Li¹, X. B. Li¹, X. F. Li¹, Z. W. Li¹, X. H. Liang¹, J. Y. Liao¹, C. Z. Liu¹, H. X. Liu^{1,3}, H. W. Liu⁹, X. J. Liu¹, F. J. Lu^{1,3} , X. F. Lu¹, Q. Luo^{1,3} , T. Luo¹, R. C. Ma^{1,3} , B. Meng¹, Y. Nang^{1,3}, J. Y. Nie¹, G. Ou¹⁰, N. Sai^{1,3}, L. M. Song^{1,3} , X. Y. Song¹, L. Sun¹, Y. Tan¹, Y. L. Tuo^{1,3}, C. Wang^{3,11}, L. J. Wang¹¹ , P. J. Wang^{3,11}, W. S. Wang¹⁰, Y. S. Wang¹, X. Y. Wen¹, B. Y. Wu^{1,3}, B. B. Wu¹, M. Wu¹, G. C. Xiao^{1,3}, S. Xiao^{1,3} , S. L. Xiong¹, Y. P. Xu^{1,3}, S. Yang¹, Y. J. Yang¹, Q. B. Yi^{1,12}, Q. Q. Yin¹ , Y. You^{1,3}, F. Zhang⁹, H. M. Zhang¹⁰, J. Zhang¹, P. Zhang¹, W. C. Zhang¹, W. Zhang^{1,3}, Y. F. Zhang¹, Y. H. Zhang^{1,3}, H. S. Zhao¹, X. F. Zhao^{1,3}, S. J. Zheng¹, and D. K. Zhou^{1,3}

¹ Key Laboratory of Particle Astrophysics, Institute of High Energy Physics, Chinese Academy of Sciences, 19B Yuquan Road, Beijing 100049, People's Republic of China; buqc@ihep.ac.cn, bu@astro.uni-tuebingen.de

² Institut für Astronomie und Astrophysik, Kepler Center for Astro and Particle Physics, Eberhard Karls Universität, Sand 1, D-72076 Tübingen, Germany

³ University of Chinese Academy of Sciences, Chinese Academy of Sciences, Beijing 100049, People's Republic of China

⁴ INAF-Osservatorio Astronomico di Brera, Via E. Bianchi 46, I-23807 Merate (LC), Italy

⁵ Department of Physics and Astronomy, University of Southampton, Southampton, SO17 1BJ, UK

⁶ Department of Physics, Xiangtan University, Xiangtan 411105, Hunan, People's Republic of China

⁷ Department of Astronomy, Beijing Normal University, Beijing 100075, People's Republic of China

⁸ Department of Astronomy, Tsinghua University, Beijing 100084, People's Republic of China

⁹ Institute of High Energy Physics, Chinese Academy of Sciences, 19B Yuquan Road, Beijing 100049, People's Republic of China

¹⁰ Computing Division, Institute of High Energy Physics, Chinese Academy of Sciences, 19B Yuquan Road, Beijing 100049, People's Republic of China

¹¹ Key Laboratory of Space Astronomy and Technology, National Astronomical Observatories, Chinese Academy of Sciences, Beijing 100012, People's Republic of China

¹² School of Physics and Optoelectronics, Xiangtan University, Xiangtan 411105, Hunan, People's Republic of China

Received 2020 December 1; revised 2021 June 28; accepted 2021 July 5; published 2021 September 29

Abstract

We report the energy-resolved broadband timing analysis of the black hole X-ray transient MAXI J1631-479 during its 2019 outburst from February 11 to April 9, using data from the Insight–Hard X-ray Modulation Telescope (Insight-HXMT), which caught the source from its hard-intermediate state to the soft state. Thanks to the large effective area of Insight-HXMT at high energies, we are able to present the energy dependence of fast variability up to ~ 100 keV. Type-C quasi-periodic oscillations (QPOs) with a frequency varying between 4.9 and 6.5 Hz are observed in the 1–100 keV energy band. While the QPO fractional rms increases with photon energy from 1 keV to ~ 10 keV and remains more or less constant from ~ 10 keV to ~ 100 keV, the rms of the flat-top noise first increases from 1 keV to ~ 8 keV and then drops to less than 0.1% above ~ 30 keV. We suggest that the disappearance of the broadband variability above 30 keV could be caused by the nonthermal acceleration in the Comptonizing plasma. At the same time, the QPOs could be produced by the precession of either a small-scale jet or a hot inner flow model.

Unified Astronomy Thesaurus concepts: [Stellar accretion disks \(1579\)](#); [Low-mass x-ray binary stars \(939\)](#); [Black hole physics \(159\)](#)

1. Introduction

Galactic black hole transients (BHTs) are discovered mostly as X-ray transients, most of which are low-mass X-ray binaries. A typical outburst of a BHT lasts from months to years, displaying a characteristic evolution in its X-ray spectral and timing properties, which are further divided into different spectral states (Remillard & McClintock 2006; Belloni & Motta 2016). Low frequency quasi-periodic oscillations (LFQPOs) are commonly observed in BHTs. They are observed as narrow peaks in the Fourier power density spectra (PDS) computed from the fast variable light curves. In BH systems, the LFQPOs are known as types A, B, and C (Casella et al. 2005; Motta et al. 2015), with frequency varying from a few mHz to tens of hertz. The relation between X-ray variability and spectral state

evolution in BHTs has been addressed in plenty of works, making fast variability an indicator that traces the spectral states during an outburst (Belloni et al. 2011).

A clear pattern of the X-ray spectral evolution is found in most BHTs, known as the “q-diagram” (Homan et al. 2001; Belloni & Motta 2016). For a typical BHT outburst, the source starts from the low hard state (LHS) and lasts over a wide range of luminosity before it evolves into the hard-intermediate state (HIMS). During the LHS, the X-ray spectrum is dominated by a nonthermal emission from an optical/thin corona (Done et al. 2007; Gilfanov 2010; Belloni & Motta 2016). The disk component starts becoming important in the X-ray flux during the HIMS. Type-C QPOs characterized by a high amplitude (up to $\sim 20\%$ rms) and simultaneous “flat-top” noise (FTN) are observed in the LHS and HIMS and their frequencies correlate

tightly with the spectral photon index (Vignarca et al. 2003). The soft intermediate state (SIMS) is usually recognized by the appearance of type-B QPOs, since the energy spectra from the softest HIMS and the SIMS are indistinguishable (at least below ~ 10 keV) when their hardness ratios are similar (Stiele et al. 2011). However, for each single source the hardness of the SIMS is always lower than in the HIMS. Type-B QPOs are characterized by a relatively high amplitude (up to $\sim 5\%$ rms) and a weak red noise, thereby making them distinguishable from type-C QPOs (Remillard et al. 2002; Casella et al. 2005; Ingram & Motta 2019). When the disk component becomes dominant in the energy spectra, the source transitions into the soft state (SS) from the SIMS. Type-A QPOs very rarely appear in the SS and have a very weak rms (a few percent rms). Eventually, the source enters into the LHS again after passing through the intermediate states in a reverse order.

MAXI J1631-479 is an X-ray binary transient discovered by the Monitor of All-sky X-ray Image (MAXI) (Kobayashi et al. 2018) on 2018 December 21. The spectral properties of MAXI J1631-479 obtained with the Nuclear Spectroscopic Telescope Array (NuSTAR) indicate that the source is an accreting black hole discovered in its SS (Miyasaka et al. 2018). A soft-to-hard state transition was later observed on 2019 January 23 (MJD 58506; Negoro et al. 2019), accompanied by clear changes in the X-ray flux and variability properties (van den Eijnden et al. 2019).

Evidence for strong reflection features was detected in the X-ray energy spectra of NuSTAR observations in the SS of the outburst (Miyasaka et al. 2018; Xu et al. 2020). During the HIMS, PDS with LFQPOs and strong peak noise were observed by the Neutron Star Interior Composition Explorer, (NICER; van den Eijnden et al. 2019; Rout et al. 2021). The detected QPO frequency varies between ~ 4 Hz and ~ 10 Hz, while the total fractional rms in the 0.1–100 Hz range remains at $\sim 12\%$ (3–12 keV). The QPO shows a hard phase lag of ~ 0.1 rad between the ~ 4 –6 keV and ~ 6 –10 keV energy bands, which is consistent with the QPO phase lags widely seen in low-inclination BHT systems (van den Eijnden et al. 2017). Both the spectral and timing properties strongly suggest MAXI J1631-479 is a black hole X-ray binary.

The Insight–Hard X-ray Modulation Telescope (Insight-HXMT) carried out Target of Opportunity (ToO) observations on MAXI J1631-479 following the MAXI/GSC discovery from 2019 February 11 (MJD 58526), covering two months of the outburst, for a total exposure time of ~ 300 ks. There are three main scientific payloads on board Insight-HXMT: the Low Energy Telescope (LE, 1–15 keV, 384 cm^2 , ~ 1 ms), the Medium Energy Telescope (ME, 5–30 keV, 952 cm^2 , $\sim 276\text{ }\mu\text{s}$), and the High Energy (HE, 20–250 keV, 5000 cm^2 , $\sim 25\text{ }\mu\text{s}$) Telescope (Cao et al. 2020; Chen et al. 2020; Liu et al. 2020; Zhang et al. 2020). The broadband energy coverage, high time resolution, and large effective area of Insight-HXMT make it an excellent tool in broadband spectral-timing studies of bright X-ray sources (Chen et al. 2018; Huang et al. 2018).

In this work, we report the broadband timing properties of the Insight-HXMT ToO observational campaign of MAXI J1631-479. Thanks to its high statistics in the hard X-ray band (>30 keV), we are able to perform a detailed analysis. In Section 2, we introduce the Insight-HXMT observations and our data reduction strategy. In Section 3, we present our timing analysis of these observations. We discuss the implications of our results in Section 4.

2. Observations and Data Reduction

In this work, we make use of the Insight-HXMT observations of MAXI J1631-479 from 2019 February 11 (MJD 58526) to 2019 April 9 (MJD 58582), for a total exposure time of 300 ks. The average exposure times of each observation are ~ 1.7 ks for LE, ~ 4.5 ks for ME, and ~ 3.5 ks for HE.

We process the original data using the HXMTDAS pipeline.¹³ We screen the data according to the suggested criteria of the good time intervals (GTIs) selection: elevation angle (ELV) larger than 10° ; ELV for the bright Earth larger than 30° ; geometric cutoff rigidity larger than 8 GeV; offset for the point position smaller than 0.1° ; at least 300 s before and after the South Atlantic Anomaly passage. To avoid the possible contamination from the bright Earth and nearby sources, only small fields of view (FoVs) are applied.

Light curves are extracted from screened files using the HELCGEN, MELCGEN, and LELCGEN tasks. In Figure 1, we show the net count rates for each instrument in the right panel. Observations P0214003024 and P0214003029 are excluded because of the short GTIs (<100 s), which leaves us a total of 27 observations.

2.1. Background Subtraction

The background estimations of HE, ME, and LE are performed using the stand-alone Python scripts LEBKGMAP, MEBKGMAP, and HEBKGMAP (Guo et al. 2020; Li et al. 2020; Liao et al. 2020a, 2020b). The averaged background count rate is ~ 10 cts s^{-1} for LE (1–10 keV), ~ 35 cts s^{-1} for ME (10–30 keV), and ~ 350 cts s^{-1} for HE (30–150 keV). The background levels of the three telescopes are shown as gray lines in Figure 1.

It must be noted that there are sources in the field of MAXI J1631-479, as illustrated by the HXMT Bright Source Warning Tool,¹⁴ whose contributions cannot be modeled by the background software.

Relatively bright contaminating sources included in the small FoVs¹⁵ of MAXI J1631-479 are 4U 1608-52, GX 339-4, J161741.2-510455, and GX 340+0. Objects 4U 1608-52, GX 339-4, and J161741.2-510455 are transient sources that were in a quiescence state during the outburst of MAXI J1631-479 (see the light curves monitored by MAXI/GSC; <http://maxi.riken.jp/top/slist.html>); the background contributions from these sources are thus ignored. GX 340+0 is a persistent Z source and has fast variability, whose X-ray flux stabilizes at ~ 457 mCrab in 2–20 keV (MAXI/GSC) and ~ 40 mCrab in 15–50 keV (Swift/BAT) during our observation.

The small FoVs of Insight-HXMT consist of three Detection Boxes (DetBox No. 1, 2, and 3) for LE, ME, and HE, as shown in Figure 2. GX 340+0 constantly appears in the No.2 DetBox of the LE detector and occasionally appears in the No.2 DetBox of the ME detector and No.3 DetBox of the HE detector during our observation. In order to estimate the background contribution from GX 340+0, we create pixel-averaged light curves from each DetBox and compare the flux differences between them. The pixel-averaged light curve for the three telescopes are shown in Figure 3. Our results show that for LE (1–10 keV), the background contribution from GX 340+0 is less than 1% and can be ignored; for ME (10–30 keV), the contribution is ~ 3 cts s^{-1} and is

¹³ <http://hxmtcn.ihep.ac.cn/SoftDoc/501.jhtml>

¹⁴ <http://proposal.ihep.ac.cn/soft/soft2.jsp>

¹⁵ The small FoVs are $1.6^\circ \times 6^\circ$ for LE, $1^\circ \times 4^\circ$ for ME, and $1.1^\circ \times 5.7^\circ$ for HE.

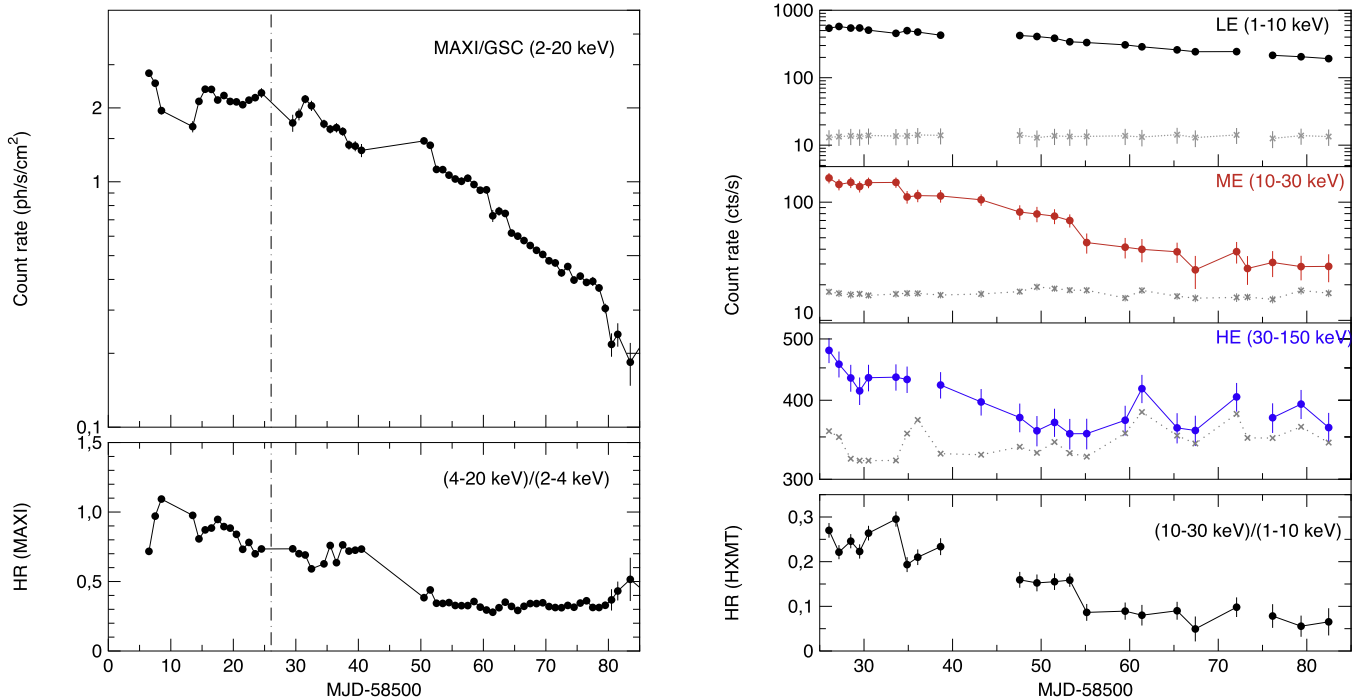


Figure 1. Left panel: (top) long-term MAXI/GSC monitoring light curve of the 2018–2019 outburst of MAXI J1631-479; (bottom) hardness ratios (HRs) are estimated as the ratio of count rates in the energy bands of 4–20 keV and 2–4 keV of MAXI. The data are binned by 24 hr. The dashed line indicates the start time of Insight-HXMT observation on the right panel. Right Panel: Insight-HXMT light curves and HRs of MAXI J1631-479. The gray lines show the background level for the three instruments. HR is estimated as the ratio of net count rates in the energy bands of 10–30 keV and 1–10 keV of Insight-HXMT. The selected energy bands and instruments are illustrated in the plot. Each point corresponds to one observation. HE data fall below the detection limit after MJD 58553.

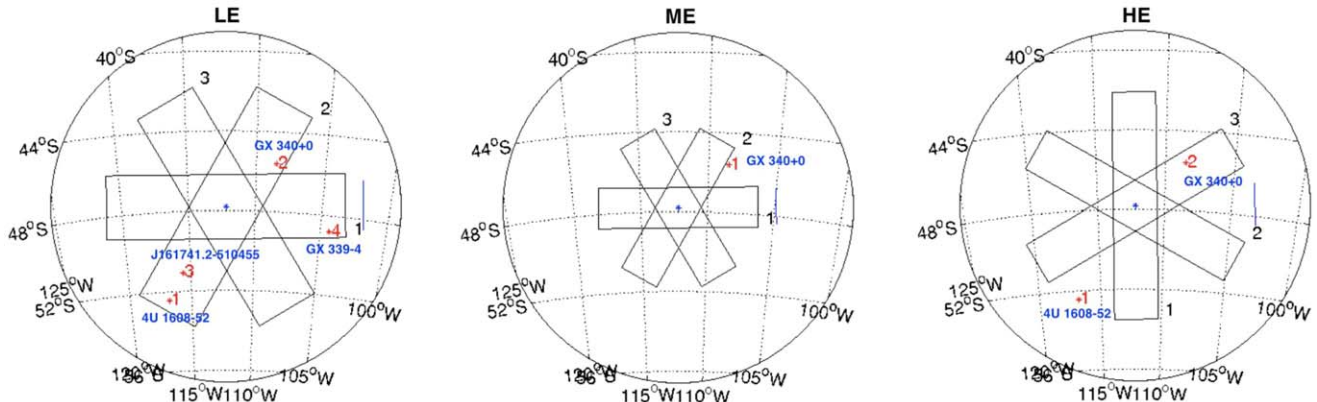


Figure 2. The small FoVs of Insight-HXMT and the location of contaminating sources compared to our target source during our observation. In order to estimate the contribution of GX 340+0, we create pixel-averaged light curves from each DetBox and compare the flux differences from the three telescopes. The results are shown in Figure 3.

corrected accordingly for the light curves; for HE (30–150 keV), the averaged contribution is $\sim 1 \text{ cts s}^{-1}$, with a maximum contribution of $\sim 5\%$. Considering the systematic error in HE, the HE background contribution from GX 340+0 is negligible.

3. Analysis and Results

3.1. Spectral Evolution

To address the spectral state evolution during our Insight-HXMT observations in a broader context, we plot the long-term MAXI/GSC monitoring light curves (Figure 1, left panel). The MAXI/GSC light curve and hardness ratio are produced by the MAXI/GSC on-demand web interface.¹⁶

MAXI/GSC started the observation of MAXI J1631-479 when the source transitioned to the HIMS on MJD 58506 (Negoro et al. 2019; van den Eijnden et al. 2019; Rout et al. 2021). Insight-HXMT started the follow-up observation of this source on MJD 58526, 20 days after the first observation of MAXI/GSC while the source was still in the HIMS, which is indicated as the dashed line in the left panel of Figure 1.

Significant spectral variability is found in the light curves of Insight-HXMT, where the count rate in the hard X-ray band ($> 10 \text{ keV}$) decreases by a factor of ~ 3 and the soft X-ray band ($< 10 \text{ keV}$) decreases by a factor of ~ 1.2 . The count rate in the 30–150 keV band becomes undetectable near MJD 58553, suggesting a major reduction from the hard X-ray emission. It is clear that Insight-HXMT caught MAXI J1631-479 in the HIMS, when the source shows relatively high variability.

¹⁶ http://maxi.riken.jp/star_data/J1631-478/J1631-478.html

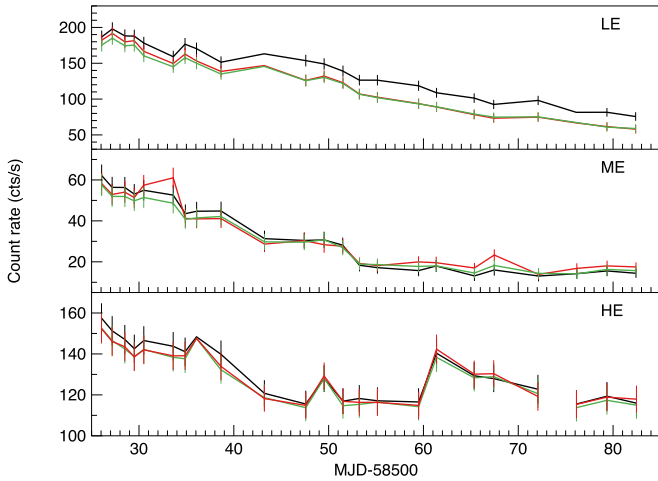


Figure 3. The pixel-averaged light curves generated from the three DetBoxes of small FoVs for the three telescopes. The red lines are the ones created from the contaminating DetBox and the blue/black lines are from the other two uncontaminated DetBoxes.

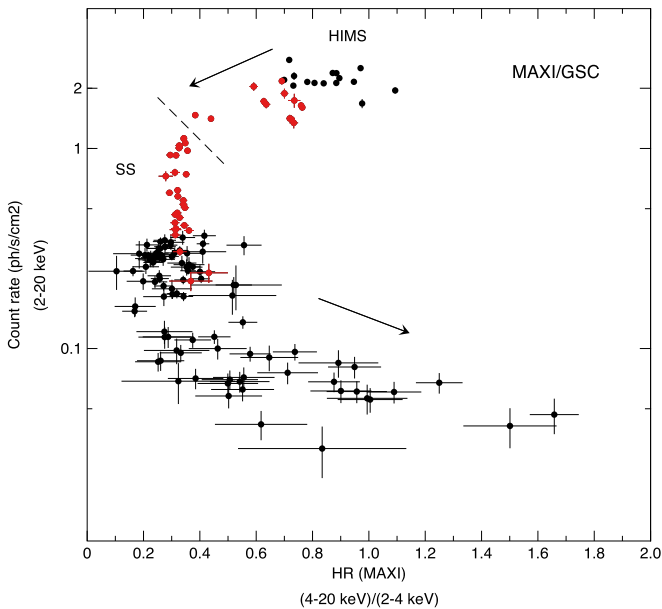


Figure 4. The hardness-intensity diagram (HID) of MAXI J1631-479 extracted from MAXI/GSC. The corresponding applied energy channels are labeled in the plot. The data points are binned by 24 hr. The red points highlight the simultaneous Insight-HXMT observations. The dashed line separates the HIMS from the SS and the arrows indicate the evolution path of the outburst.

The hardness-intensity diagram (HID, also known as the “q-diagram”) of Figure 4 reports data from MAXI/GSC since the source transitioned into the HIMS. In the HID, the hardness ratio is defined between the energy bands 4–20 keV and 2–4 keV. The simultaneous Insight-HXMT observational period is highlighted in red. Both MAXI and Insight-HXMT have missed the initial rising phase of the outburst; thus, both HIDs are incomplete. In Figure 4, the hardness ratio decreases from ~ 1.1 to ~ 0.5 during the first ~ 40 days, while the source flux (2–20 keV) varies slightly near ~ 2 photons $\text{s}^{-1} \text{cm}^{-2}$, suggesting that the source is still in the HIMS. Subsequently, the flux drops abruptly from ~ 2.0 to ~ 0.2 photons $\text{s}^{-1} \text{cm}^{-2}$, while the hardness ratio stays constant at ~ 0.3 , suggesting that the source may have entered the SS.

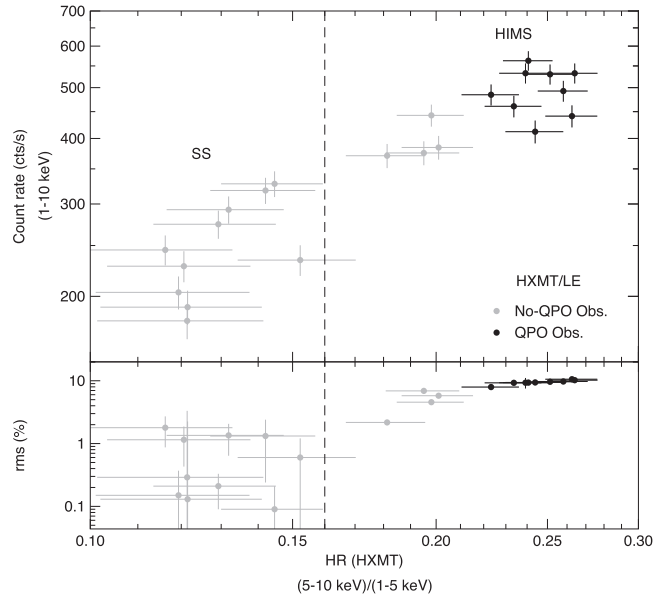


Figure 5. Hardness-intensity and hardness-rms diagram produced from the Insight-HXMT/LE. The spectral hardness ratio is defined between 5–10 keV and 1–5 keV energy bands. The total fractional rms is averaged in frequency range 0.1–32 Hz for 1–10 keV. The vertical dashed line separates the HIMS and SS. The QPO observations are highlighted in black. The data are binned by each observation.

In order to study the state transition in detail, we calculate the total fractional rms in the 1–32 Hz frequency range for 1–10 keV using the Insight-HXMT/LE observation. In Figure 5, we show the HID and hardness-rms diagram (HRD) from the LE. The hardness ratio for LE is defined between the energy bands 5–10 keV and 1–5 keV. The QPO observations are highlighted in black. The HID of HXMT/LE shows a behavior similar to that of MAXI/GSC. In addition, the corresponding total fractional rms (1–32 Hz, 1–10 keV) initially stays at $\sim 9.5\%$ for ~ 15 days and abruptly drops to 4% near MJD 58543, accompanied with a disappearance of QPOs (see Section 3.2), which suggests that the source has left the HIMS and entered a softer state. Hereafter, the total rms varies between 4% and 6%, while the corresponding hardness ratio remains at ~ 0.2 . During which, the band-limited noise disappears and is replaced by a power-law noise. The total rms drops to less than 1% after MJD 58553 when the emission from >10 keV decreases to less than 10 cts s^{-1} , suggesting that the source may have entered the SS (Belloni et al. 2005; Heil et al. 2015). We therefore give an approximate division of source states based on the HID/HRD properties and mark them as dashed lines in the HID/HRD.

3.2. Power Density Spectra

For each of the three instruments, we extract an average PDS from each observation by dividing the data into 32 s intervals and averaging the corresponding PDS. The time resolution is 1 ms corresponding to a Nyquist frequency of 500 Hz. The PDS are normalized according to Leahy et al. (1983) and the component due to Poissonian statistics was subtracted according to Zhang et al. (1995).

The selected energy bands are 1–10 keV for LE, 10–30 keV for ME, and 30–150 keV for HE, respectively. The PDS fittings are performed with XSPEC (12.10.1f), by applying a one-to-one

Table 1
Best-fitting Parameters of the QPO Observations of MAXI J1631-479 Extracted from Insight-HXMT

ID	MJD	Exp (ks)	rms _{total}	ν (Hz)	FWHM (Hz)	rms _{QPO}
LE (1–10 keV)						
P0214003002	58526.0	0.9	10.2 ± 0.3	5.0 ± 0.1	1.0 ± 0.2	5.6 ± 0.4
P0214003003	58527.1	0.8	9.4 ± 0.3	6.1 ± 0.1	$1.1^{+0.4}_{-0.3}$	$4.7^{+0.5}_{-0.4}$
P0214003004	58528.4	1.4	9.6 ± 0.3	5.4 ± 0.1	1.4 ± 0.3	5.3 ± 0.4
P0214003005	58529.4	1.6	$9.3^{+0.4}_{-0.2}$	6.2 ± 0.1	0.9 ± 0.3	4.1 ± 0.5
P0214003006	58530.4	1.9	9.7 ± 0.2	5.2 ± 0.1	$0.9^{+0.2}_{-0.1}$	5.1 ± 0.3
P0214003007	58533.5	2.1	10.6 ± 0.2	4.9 ± 0.1	0.9 ± 0.2	4.8 ± 0.3
P0214003008	58534.8	2.7	8.0 ± 0.2	6.9 ± 0.1	$1.8^{+0.6}_{-0.5}$	4.0 ± 0.4
P0214003009	58536.0	1.3	9.3 ± 0.3	6.1 ± 0.1	$0.5^{+0.4}_{-0.3}$	2.6 ± 0.6
P0214003010	58538.6	2.5	9.4 ± 0.2	5.4 ± 0.1	$0.5^{+0.2}_{-0.1}$	3.6 ± 0.4
P0214003011	58541.2
ME (10–30 keV)						
P0214003002	58526.0	3.1	$13.2^{+0.4}_{-0.5}$	5.0 ± 0.1	0.9 ± 0.1	$10.0^{+0.5}_{-0.4}$
P0214003003	58527.1	2.0	$14.8^{+0.6}_{-0.7}$	$6.1^{+0.1}_{-0.02}$	0.9 ± 0.2	9.6 ± 0.6
P0214003004	58528.4	3.2	13.8 ± 0.6	5.5 ± 0.04	0.9 ± 0.1	9.6 ± 0.5
P0214003005	58529.4	3.3	$13.8^{+0.5}_{-0.6}$	6.2 ± 0.04	0.7 ± 0.1	8.7 ± 0.5
P0214003006	58530.4	3.2	$13.6^{+0.5}_{-0.6}$	$5.2^{+0.01}_{-0.02}$	0.4 ± 0.1	8.4 ± 0.4
P0214003007	58533.5	5.5	$17.9^{+0.3}_{-0.4}$	$4.8^{+0.05}_{-0.04}$	0.6 ± 0.1	$7.6^{+0.4}_{-0.5}$
P0214003008	58534.8	8.6	$13.8^{+0.4}_{-0.5}$	6.6 ± 0.1	$2.8^{+0.2}_{-0.8}$	$13.0^{+1.1}_{-2.2}$
P0214003009	58536.0	6.6	$13.5^{+0.4}_{-0.5}$	6.2 ± 0.04	0.9 ± 0.1	$9.5^{+0.5}_{-0.4}$
P0214003010	58538.6	4.9	$11.8^{+0.6}_{-0.7}$	5.4 ± 0.1	0.8 ± 0.1	9.1 ± 0.5
P0214003011	58541.2	4.2	$14.3^{+0.6}_{-0.3}$	6.2 ± 0.1	$1.5^{+0.3}_{-0.2}$	$10.0^{+0.5}_{-0.3}$
HE (30–150 keV)						
P0214003002	58526.1	2.0	15.8 ± 0.6	5.3 ± 0.04	0.6 ± 0.1	8.7 ± 0.6
P0214003003	58527.1	1.0	$15.8^{+1.8}_{-1.2}$	6.2 ± 0.1	$0.7^{+0.3}_{-0.2}$	$8.3^{+1.1}_{-1.0}$
P0214003004	58528.4	3.2	$16.3^{+0.7}_{-0.6}$	5.5 ± 0.1	1.2 ± 0.3	$8.9^{+0.8}_{-0.7}$
P0214003005	58529.4	3.5	$17.8^{+0.6}_{-0.7}$	6.1 ± 0.04	0.6 ± 0.1	8.9 ± 0.5
P0214003006	58530.4	3.5	$16.0^{+0.5}_{-0.6}$	5.3 ± 0.02	0.4 ± 0.1	8.2 ± 0.5
P0214003007	58533.5	5.9	$16.2^{+0.4}_{-0.5}$	$4.9^{+0.04}_{-0.03}$	0.6 ± 0.1	8.2 ± 0.4
P0214003008	58534.9	4.8	16.3 ± 0.6	6.4 ± 0.1	1.3 ± 0.3	$8.9^{+0.3}_{-0.8}$
P0214003009	58536.0
P0214003010	58538.6	4.3	$15.0^{+0.9}_{-0.8}$	5.6 ± 0.1	$1.0^{+0.3}_{-0.2}$	$8.1^{+0.8}_{-0.7}$
P0214003011	58541.2	4.3	$17.0^{+0.4}_{-0.5}$	6.4 ± 0.1	1.6 ± 0.05	$8.3^{+0.9}_{-0.8}$

Note. The table shows the observation starting time (MJD), effective exposure time (Exp), total fractional rms (rms_{total}) averaged in the 0.1–32 Hz frequency band, QPO centroid frequency (ν), QPO full width at half maximum (FWHM) and QPO fractional rms (rms_{QPO}) for the three telescopes. The errors are estimated with 1σ level uncertainties. The energy bands selected for study are 1–10 keV for the LE, 10–30 keV for the ME, and 30–150 keV for the HE. The details on the extraction of the power density spectra and on the fitting procedures are described in Section 3.2. Ellipses (...) represent empty GTIs.

energy–frequency conversion with a unit response. Both broadband noise and QPO peaks in the PDS are fitted with Lorentzian functions (Nowak 2000; Belloni et al. 2002). We use two Lorentzian peaks for the QPO and its harmonic, and one or two Lorentzian for the broadband noise. Based on the fitting results, we exclude features with a significance¹⁷ of less than 3σ or a Q factor¹⁸ of less than 2.

Among 27 observations, LFQPOs are observed in the first ten observations, as indicated with black dots in the HID of Figure 5. The fitting results of these QPOs are given in Table 1. Among all of the observations, QPOs are observed

simultaneously in eight observations by all three telescopes, with their centroid frequencies varying between ~ 4.9 Hz and ~ 6.5 Hz. While the QPO frequency remains more or less constant with energy, the QPO fractional rms first increases from the LE (1–10 keV) to ME (10–30 keV) then slightly decreases from the ME (10–30 keV) to HE (30–150 keV). Meanwhile, the total fractional rms increases monotonically with energy from 1 keV to 150 keV.

All QPOs are observed with an FTN, featuring the characteristics of type-C QPOs, which confirms that these observations correspond to the HIMS. In Figure 6, we show the PDS of ObsID P0214003006¹⁹ extracted from the three instruments. The other QPO observations show similar properties, as listed in Table 1.

¹⁷ The significance of QPOs is given as the ratio of the integral of the power of the Lorentzian used to fit the QPO divided by the negative 1σ error on the integral of the power.

¹⁸ $Q = \nu/\text{FWHM}$, where ν is the centroid frequency of the Lorentzian component and FWHM is its full width at half maximum.

¹⁹ This observation is selected because of its high count rate and long exposure time.

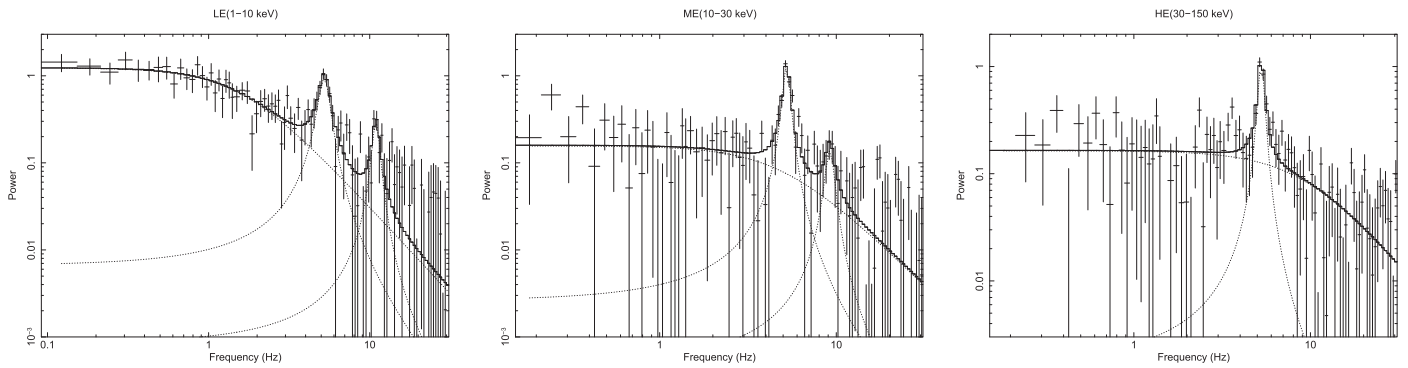


Figure 6. Power density spectra (PDS) of Observation P0214003006 extracted from 1–10 keV (left), 10–30 keV (middle), and 30–150 keV (right), respectively. A multi-Lorentzian function is applied to fit the spectra. The best-fitting lines are shown in the plots. A QPO signal at ~ 5.2 Hz is observed for all three telescopes. The error bars show the 1σ level uncertainties.

Table 2

Energy Selections for the Energy Dependence Study of MAXI J1631-479 using Insight-HXMT

Instrument	Energy Range (keV)
LE	1–5
LE	5–10
ME	8–12
ME	12–20
HE	28–40
HE	35–45
HE	45–95

3.3. Energy-dependent Power Spectra

In order to study energy dependence of the QPO parameters, we divide the 1–100 keV energy range into seven energy intervals to create the corresponding PDS. Given the good statistics of the LE and ME, we divide them into four energy intervals by ~ 5 keV. Due to the low signal-to-noise ratio of HE, we enlarge the energy bins of HE to get better statistics. The selection of energy ranges are given in Table 2.

Among 10 QPO observations, in only four observations (P0214003002, P0214003005, P0214003006, and P0214003007) is the QPO detected in all sub-energy bands with a significance of $>3\sigma$. Figure 7 shows the QPO fractional rms as a function of energy from 1 keV to ~ 100 keV. It is worth noticing that the last points from the four observations show large error bars; we suggest that the QPO fractional rms remains more or less constant from ~ 10 keV to ~ 100 keV.

The fractional rms of the FTN component is plotted in Figure 8. The FTN becomes extremely weak in the high energy band (above 30 keV). In order to give an upper limit of the FTN rms, we fix the break frequency of the FTN at ~ 1 Hz, based on the correlation ($\nu_{\text{QPO}} = (5.2 \pm 0.32) * \nu_{\text{break}}^{(0.81 \pm 0.03)}$) between LFQPO and break frequency of BHs (Wijnands & van der Klis 1999; Bu et al. 2017). The thick gray bar gives an averaged upper limit of the FTN rms given at the 1σ level. The rms of FTN generally increases with energy from ~ 1 keV, reaches its maximum near ~ 8 keV, and then decreases to $<0.1\%$ above 30 keV.

In order to compare the rms versus energy results, we also make use of the data from NICER on board the International Space Station (ISS) between 2019 February 11 and April 9, covering the interval of Insight-HXMT observations, for a total of 35 observations. The X-Ray Timing Instrument of NICER

consists of 56 X-ray optics with silicon detectors and provides high time resolution data in the 0.2–12 keV energy range (Gendreau et al. 2012). We process the original data using the NICERDAS pipeline. For each observation, we extract PDS averaging intervals of 13.1072 s over the energy range 0.2–12 keV. PDS similar to those shown in Figure 6 are observed from the first observation until March 3 (MJD 58545). From the next observation, on March 18 (MJD 58560), the PDS are consistent with the SS.

We analyze in more detail the observation with the best statistics, observation 1,200,500,127 on February 11 (MJD 58525). We extract PDS in eight separate energy bands and fit them with a multi-Lorentzian model. Given the high statistics, three harmonically related QPO peaks are seen, in addition to an FTN component and an additional broadband component at higher frequencies. The QPO main peak is at 4.45 Hz. No clear signal is detected below 1.5 keV despite the high statistics, and no QPO is detected in the last PDS, 8–12 keV, due to the lack of sensitivity. The rms versus energy for the FTN component and main QPO peak are shown as gray points in Figures 8 and 7. They are compatible with the LE and ME results.

The lag-energy spectra of type-C QPO are also studied with Insight-HXMT. Background-subtracted light curves from seven sub-energy bands are generated to calculate the cross-spectra. We extract the complex-valued product of the Fourier transforms used for PDS and produce six cross-spectra using 1–5 keV as a reference band. The correction for cross-channel talk is included by subtracting the average value of the real part of the cross-spectra in 400–500 Hz frequency range, although this is found to be negligible.

The frequency range used for the QPO time lag calculation is the QPO FWHM centered on its centroid frequency. We define hard lag (hard photons lagging soft photons) as positive lag. In order to improve the statistics, we group the QPO observations into three groups according to QPO frequency and average the time lag for each group. The lag-energy spectra for the three groups are shown in Figure 9. The QPO time lags generally show hard lags for the whole energy band with a maximum value of ~ 4 ms, except for the two points near ~ 40 keV showing soft lags. However, considering the large errors of the two points, no solid soft lags can be confirmed.

4. Discussion

We have reported the energy-resolved timing analysis of the black hole X-ray transient MAXI J1631-479 using data from

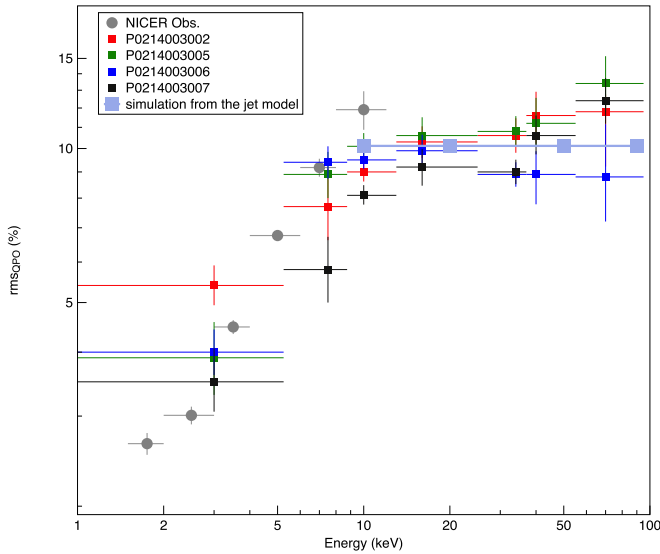


Figure 7. The QPO fractional rms as a function of photon energy. The corresponding observation IDs are indicated in the plot. The errors are given at 1σ level.

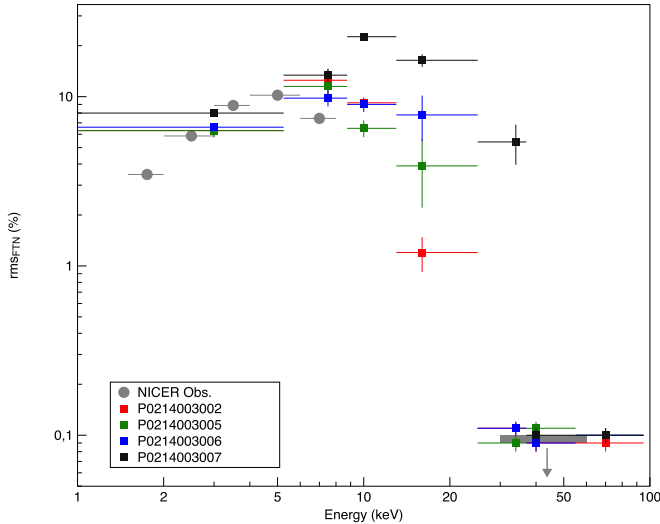


Figure 8. The fractional rms of the “flat-top” noise as a function of photon energy. The corresponding observation IDs are indicated in the plot. The errors are given at the 1σ level. The gray bar gives an averaged upper limit of the FTN rms.

the Insight-HXMT and NICER. A state transition from the intermediate state to the SS is observed near MJD 58553. The source stays for ~ 50 days in the intermediate state before it enters the SS, characterized by an abrupt drop in the total variability from $\sim 9.5\%$ rms to $\sim 1\%$ rms. Type-C QPOs with frequencies between 4.9 Hz and 6.5 Hz are observed during the HIMS. While the QPO fractional rms first increases with energy from ~ 1 keV to ~ 10 keV and remains more or less constant from ~ 10 keV to ~ 100 keV, the fractional rms of the “flat-top” noise accompanied with the type-C QPO increases with energy from ~ 1 keV to ~ 8 keV and then decreases to $< 0.1\%$ above 30 keV. The type-C QPOs generally show hard lags for the whole energy band, with a maximum value of ~ 4 ms.

Insight-HXMT started the observation of MAXI J1631-479 in its HIMS state where the source showed a high timing

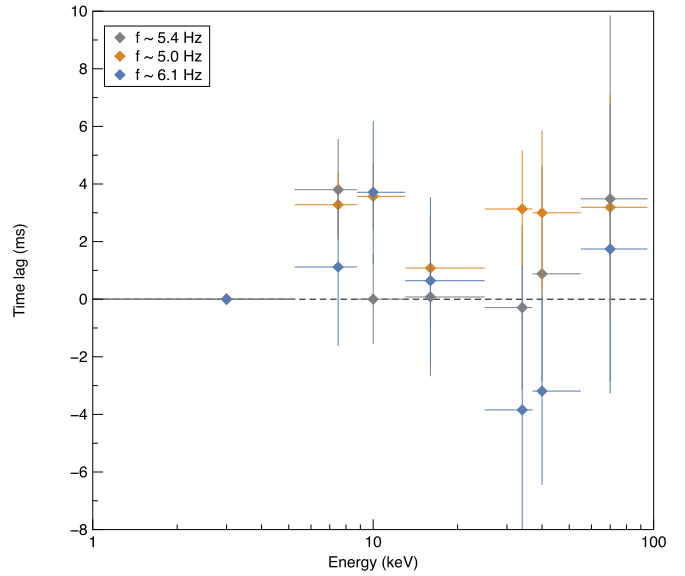


Figure 9. The QPO time lag as a function of photon energy. The corresponding QPO centroid frequencies f are indicated in the plot. The error are given at the 1σ level.

variability ($> 10\%$ rms) and the presence of a type-C QPO. The spectral state evolution is well described by the HID/HRD plot in Figure 4 and Figure 5, revealing a typical state evolution of a BHT from its HIMS to the SS. In proximity to the HIMS/SIMS transition, timing properties constitute the sole way to distinguish between HIMS/SIMS/SS, given the absence of differences in the spectral shape. Generally, the fractional rms decreases during the state transition and is very low in the SS (Belloni 2010), which helps us to distinguish the SS from the intermediate state based on the HRD correlation in Figure 5. During the late HIMS, the total fractional rms drops from $> 10\%$ to $\sim 5\%$ after MJD 58043, accompanied by a transition of broadband noise to power-law noise and a drop in hardness ratio, which could suggest a transition to the SIMS. However, the lack of type-B QPOs during this period makes the identification of SIMS less credible.

The energy spectra of BHTs are generally composed of a soft component associated with an accretion disk and a hard component resulting from Comptonization in a corona. It has been known for years that variability is mainly associated with the hard component rather than the disk. The broadband noise is generally believed to rise from propagation of fluctuations in the mass accretion rate produced at different radii (Uttley et al. 2005; Ingram & van der Klis 2013) and is known to have a soft spectrum in the hard states (Gierlinski & Zdziarski 2005). Behavior of the broadband noise rms–energy correlation similar to that of MAXI J1631-479 (Figure 8) has been found in GX 339-4 when the source was in its late HIMS (Belloni et al. 2011). The broadband noise rms increases during 1–10 keV and slightly decreases from ~ 10 keV to 20 keV. Comparing to our results from Insight-HXMT and NICER, we note that the FTN rms already starts to decrease near ~ 8 keV and drops to $< 0.1\%$ above 30 keV. These patterns can be explained by considering little variability when the disk dominates below ~ 5 keV. Above 5 keV, where the variable power law dominates, the rms values increase and remain high. When the energy is higher than 8 keV, the variability of the broadband noise decreases until it reaches the extremely low rms values ($< 0.1\%$) in the 30–100 keV band, which can be

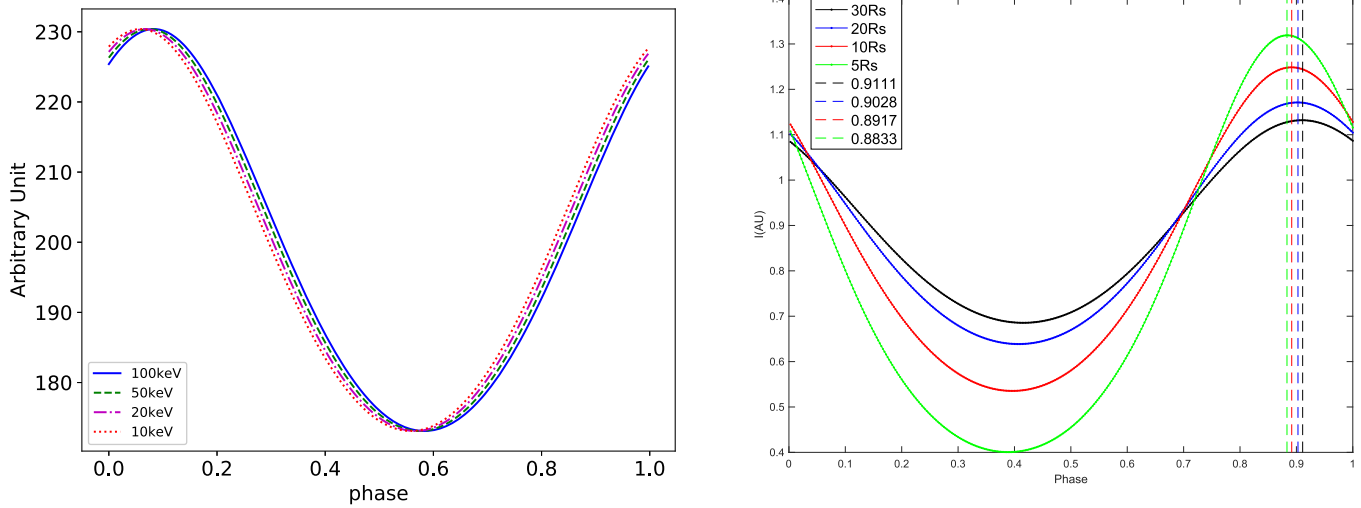


Figure 10. Simulated light curve from the LT-jet model (left) and the LT-hot flow model (right), assuming an inclination angle of $29 \pm 1^\circ$ and a misalignment angle of 10° for both models. Different colors show the simulated flux from different energy bands, while the phase differences among these waveforms give the simulated phase lags. In both models, the observed fluxes are modulated by the Doppler boosting and solid angle effect. Left: the fluxes are simulated by the observed intensity from different energy bands. Right: the fluxes are simulated for the hot flow extending from 5 to 30 R_s , which approximately represents the fluxes from 100 keV to 10 keV. The vertical lines indicate the peak phase values for the four QPO waveforms.

explained by the effect of nonthermal acceleration in the hot plasma. This effect is dominated by the Compton cooling; the electrons in the hard state are efficiently thermalized even when the power provided to them is entirely in the form of nonthermal acceleration (Zdziarski et al. 1990; Coppi 1999). In this scenario, a varying seed photon temperature and optical depth of the Comptonizing plasma could lead to the decrease of variability from ~ 10 keV to ~ 100 keV (Gierlinski & Zdziarski 2005).

Although the physical origin of type-C QPOs is still under debate, many pieces of evidence have suggested a geometric origin (Gilfanov 2010). Type-C QPOs are particularly prominent in the HIMS of BHTs and are widely believed to result from the Lense–Thirring (LT) precession of a radially extended section of the hot inner flow (Stella & Vietri 1998; Ingram et al. 2009). This geometric origin of type-C QPOs is further supported by the inclination dependence studies of the QPO characteristics, i.e., the correlations between the QPO rms (Schnittman et al. 2006; Motta et al. 2015), the sign of the energy-dependent lags (van den Eijnden et al. 2017), and the orbital inclination.

The type-C QPO rms–energy correlation in the 2–30 keV range has been extensively studied with Rossi-XTE for the last two decades, while similar energy dependence relations are found in GRS 1915+015 (Rodriguez et al. 2004; Yan et al. 2012; Yadav et al. 2016), H1743-322 (Li et al. 2013a), XTE J1859+226 (Casella et al. 2004), and XTE J1550-564 (Li et al. 2013b). The QPO rms in these sources is found to increase with energy below 10 keV and become flat above 10 keV, which is similar to the energy dependence relation we found in MAXI J1631-479. You et al. (2018) simulated the fractional rms spectra of the type-C QPOs under the framework of the LT precession model and suggested that the flattening above 10 keV is caused by the high orbital inclination angle. However, both a NuSTAR spectral analysis (Xu et al. 2020) and NICER time lag studies (van den Eijnden et al. 2019) suggest that MAXI J1631-479 is likely to be a low-inclination system that should have an increasing QPO rms with energy as predicted by You et al. (2018). Our result shows that the QPO

rms increases from 1 keV to 10 keV and becomes flat from 10 keV to 100 keV, which is inconsistent with the prediction of You et al. (2018).

Thanks to the large effective area of Insight-HXMT at high energies, we are able to extend the QPO study up to hundreds of keV, which has rarely been explored by previous satellites. A similar rms–energy dependence relation above 30 keV (see Figure 7) has been found in GRS 1915+105 with Rossi-XTE (Tomsick & Kaaret 2001), MAXI J1535-571 (Huang et al. 2018) and MAXI J1820+070 (Ma et al. 2021) with Insight-HXMT, in which geometric origins of type-C QPO are suggested. The large soft lag (~ 0.9 s) above 200 keV and energy-related behaviors of the type-C QPOs found in MAXI J1820+070 have posed a great challenge for the existing models (Ma et al. 2021). Ma et al. (2021) proposed a model based on the LT precession of a small-scale jet to describe the origin of type-C QPOs, in which the jet twists and rotates around the BH spin axis and the Doppler boosting and solid angle effect modulate the observed flux. In this process, LFQPOs at different energies would be produced from the different parts of the jet with the same frequency. The rms of the LFQPO (i.e., the amplitude of variability in the observed flux) depends on the jet speed (v) and the jet projected angle along the line of sight (θ). The phase lag solely depends on the difference in the projected jet angle on the X - Y plane that is perpendicular to the BH spin axis.










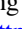





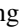
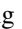

We apply the LT precession of the jet model to explain our results (the energy dependence of QPO rms and time lag) from MAXI J1631-479. Assuming an orbital inclination angle of $29 \pm 1^\circ$ (Xu et al. 2020), a misalignment angle of 10° between the BH spin axis and the jet ejection direction, and a jet speed of 0.85 – $0.9c$, the QPO fractional rms of $\sim 10\%$ above 10 keV can be reproduced (see blue squares in Figure 7). When the energy is below 10 keV, both the disk and hard components contribute to the variability; thus, the QPO rms cannot be accurately predicted by the jet model. The time lag of ~ 4 ms can also be reproduced if a small difference in the projected jet angles is considered ($\sim 3^\circ$; see the left panel in Figure 10) on the X - Y plane that is perpendicular to the BH spin axis, which suggests that the jet is

slightly curved. The jet model can also explain the timing and spectral evolution as the jet size and velocity changes. The QPO frequency increases when the height of jet decreases; meanwhile, the spectra soften as more hard photons from the jet are reflected by the accretion disk. When the source evolves to the late HIMS, the QPO rms decreases, which could be explained by the change of the jet speed.

In order to make a comparison, we also apply the LT precession of the truncated disk hot flow model to our results, in which the hot flow precesses as a solid body extending from an inner radius to the truncation radius of the cold outer disk. The observed flux is modulated by the Doppler boosting and solid angle effect to the observer. Assuming an orbital inclination angle of $29 \pm 1^\circ$, an inner radius of 5 Schwarzschild radii (R_s) and a truncation radius of 30 R_s for the hard state, the QPO fractional rms of $\sim 10\%$ above 10 keV and the QPO phase lag of $\sim 0.1\text{--}0.2$ between 1–5 keV and 45–95 keV can be reproduced (see the right panel in Figure 10). Unlike for the jet model, the phase lag depends on the observer’s azimuth and inclination angles.

We are grateful for the anonymous referee’s helpful comments and suggestions. This research has made use of the data from the Insight-HXMT mission, a project funded by China National Space Administration (CNSA) and the Chinese Academy of Sciences (CAS), and data and/or software provided by the High Energy Astrophysics Science Archive Research Center (HEASARC), a service of the Astrophysics Science Division at NASA/GSFC. This work has also made use of the MAXI data provided by RIKEN, JAXA, and the MAXI team. Q.C.B. acknowledges support from the National Program on Key Research and Development Project (grant No. 2016YFA0400801), the National Natural Science Foundation of China (grant Nos. U1838201, U1838202, 11733009, 11673023, U1838111, U1838108, and U1938102) and the China Postdoctoral Science Foundation. T.M.B. acknowledges financial contributions from the agreement ASI-INAF n.2017-14-H.0. and PRIN-INAF 2019 n.15. L.Z. acknowledges support from the Royal Society Newton Funds. Z.S.L. acknowledges support from the National Natural Science Foundation of China (U1938107). T.L. acknowledges support from the National Natural Science Foundation of China (U1838115).

ORCID iDs

Q. C. Bu  <https://orcid.org/0000-0001-5238-3988>
 S. N. Zhang  <https://orcid.org/0000-0001-5586-1017>
 L. Zhang  <https://orcid.org/0000-0003-4498-9925>
 J. L. Qu  <https://orcid.org/0000-0002-9796-2585>
 L. Tao  <https://orcid.org/0000-0002-2705-4338>
 H. Gao  <https://orcid.org/0000-0002-3100-6558>
 M. Y. Ge  <https://orcid.org/0000-0002-2749-6638>
 S. M. Jia  <https://orcid.org/0000-0002-5203-8321>
 L. D. Kong  <https://orcid.org/0000-0003-3188-9079>
 B. Li  <https://orcid.org/0000-0001-7997-4817>
 C. K. Li  <https://orcid.org/0000-0001-5798-4491>
 F. J. Lu  <https://orcid.org/0000-0003-3248-6087>
 Q. Luo  <https://orcid.org/0000-0003-1853-7810>
 R. C. Ma  <https://orcid.org/0000-0003-3260-8718>
 L. M. Song  <https://orcid.org/0000-0003-0274-3396>
 L. J. Wang  <https://orcid.org/0000-0002-8352-1359>
 S. Xiao  <https://orcid.org/0000-0003-2957-2806>
 Q. Q. Yin  <https://orcid.org/0000-0001-7580-1513>

References

- Belloni, T., Homan, J., Casella, P., et al. 2005, *A&A*, 440, 207
 Belloni, T., Psaltis, D., & van der Klis, M. 2002, *ApJ*, 572, 392
 Belloni, T. M. 2010, *LNP*, 794, 53
 Belloni, T. M., & Motta, S. E. 2016, in *Astrophysics of Black Holes: From Fundamental Aspects to Latest Developments*, Astrophysics and Space Science Library, Vol. 440 ed. C. Bambi (Berlin: Springer-Verlag), 61
 Belloni, T. M., Motta, S. E., & Muñoz-Darias, T. 2011, *BASI*, 39, 409
 Bu, Q. C., Belloni, T., Chen, L., et al. 2017, *ApJ*, 841, 122
 Cao, X. L., Jiang, W. C., Meng, B., et al. 2020, *Sci. China-Phys. Mech. Astron.*, 63, 249504
 Casella, P., Belloni, T., Homan, J., et al. 2004, *A&A*, 426, 587
 Casella, P., Belloni, T., & Stella, L. 2005, *ApJ*, 629, 403
 Chen, Y., Cui, W., Li, W., et al. 2020, *Sci China-Phys Mech Astron*, 63, 249505
 Chen, Y. P., Zhang, S., Qu, J. L., et al. 2018, *ApJL*, 864, L30
 Coppi, P. S. 1999, in *ASP Conf. Ser. 161, High Energy Processes in Accreting Black Holes*. Astron. Soc. Pac., San Francisco, ed. J. Poutanen & R. Svensson (San Francisco, CA: ASP), 375
 Done, C., Gierlinski, M., & Kubota, A. 2007, *A&ARv*, 15, 1
 Fender, R. P., & Belloni, T. M. 2004, *ARA&A*, 42, 317
 Fender, R. P., Homan, J., & Belloni, T. M. 2009, *MNRAS*, 396, 1370
 Gendreau, K. C., Arzoumanian, Z., & Okajima, T. 2012, *Proc. SPIE*, 8443, 844313
 Gierlinski, M., & Zdziarski, A. 2005, *MNRAS*, 363, 1349
 Gilfanov, M. 2010, in *X-Ray Emission from Black-Hole Binaries*, ed. T. Belloni, Vol. 794 (Berlin, Heidelberg: Springer)
 Guo, C. C., Liao, J. Y., Zhang, S., et al. 2020, *JHEAp*, 27, 44
 Heil, L. M., Uttley, P., & Klein-Wolt, M. 2015, *MNRAS*, 448, 3339
 Homan, J., Wijnands, R., van der Klis, M., et al. 2001, *ApJS*, 132, 377
 Huang, Y., Qu, J. L., Zhang, S. N., et al. 2018, *ApJ*, 866, 122
 Ingram, A., Done, C., & Fragile, P. C. 2009, *MNRAS*, 397, L101
 Ingram, A., & van der Klis, M. 2013, *MNRAS*, 434, 1476
 Ingram, A. R., & Motta, S. E. 2019, *NewAR*, 85, 101524
 Kobayashi, K., Maruyama, W., Negoro, H., et al. 2018, *ATel*, 12320, 1
 Leahy, D. A., Elsner, R. F., & Weisskopf, M. C. 1983, *ApJ*, 272, 256
 Li, X., Li, X., Tan, Y., et al. 2020, *JHEAp*, 27, 64
 Li, Z. B., Qu, J. L., Song, L. M., et al. 2013b, *MNRAS*, 428, 1704
 Li, Z. B., Zhang, S., Qu, J. L., et al. 2013a, *MNRAS*, 433, 412
 Liao, J. Y., Zhang, S., Chen, Y., et al. 2020a, *JHEAp*, 27, 24
 Liao, J. Y., Zhang, S., Chen, Y., et al. 2020b, *JHEAp*, 27, 14
 Liu, C. Z., Zhang, Y. F., Li, X. F., et al. 2020, *Sci. China-Phys. Mech. Astron.*, 63, 249503
 Ma, X., Tao, L., Zhang, S. N., et al. 2021, *NatAs*, 5, 94
 Miller-Jones, J. C. A., Sivakoff, G. R., Altamirano, D., et al. 2012, *MNRAS*, 421, 468
 Miyasaka, H., Tomsick, J., Xu, Y., et al. 2018, *ATel*, 12340, 1
 Motta, S. E., Casella, P., Henze, M., et al. 2015, *MNRAS*, 447, 2059
 Negoro, H., Nakajima, M., Sakamaki, A., et al. 2019, *ATel*, 12421, 1
 Nowak, M. A. 2000, *MNRAS*, 318, 361
 Remillard, R. A., & McClintock, J. E. 2006, *ARA&A*, 44, 49
 Remillard, R. A., Sobczak, G. J., Munro, M. P., et al. 2002, *ApJ*, 564, 962
 Rodriguez, J., Corbel, S., Hannikainen, D. C., et al. 2004, *ApJ*, 615, 416
 Rout, S. K., Méndez, M., Belloni, T., et al. 2021, *MNRAS*, 505, 1213
 Schnittman, J. D., Homan, J., & Miller, J. M. 2006, *ApJ*, 642, 420
 Stella, L., & Vietri, M. 1998, *ApJ*, 492, L59
 Stevens, A. L., & Uttley, P. 2016, *MNRAS*, 460, 2796
 Stiele, H., Motta, S., Muñoz-Darias, T., & Belloni, T. M. 2011, *MNRAS*, 418, 1746
 Tomsick, J. A., & Kaaret, P. 2001, *ApJ*, 548, 401
 Uttley, P., McHardy, I. M., & Vaughan, S. 2005, *MNRAS*, 359, 345
 van den Eijnden, J., Ingram, A., Uttley, P., et al. 2017, *MNRAS*, 464, 2643
 van den Eijnden, J., Ludlam, R. M., Homan, J., et al. 2019, *ATel*, 12440, 1
 Vignarca, F., Migliari, S., Belloni, T., et al. 2003, *A&A*, 397, 729
 Wijnands, R., & van der Klis, M. 1999, *ApJ*, 514, 939
 Xu, Y., Harrison, F., Tomsick, J., et al. 2020, *ApJ*, 893, 30
 Yadav, J. S., Misra, R., Verdhhan, J., et al. 2016, *ApJ*, 833, 27
 Yan, S. P., Qu, J. L., Ding, G. Q., et al. 2012, *Ap&SS*, 337, 137
 You, B., Bursa, M., & Zycki, P. T. 2018, *ApJ*, 858, 82
 Zdziarski, A. A., Coppi, P. S., & Lamb, D. Q. 1990, *ApJ*, 357, 149
 Zhang, S. N., Li, T. P., Lu, F. J., et al. 2020, *Sci. China-Phys. Mech. Astron.*, 63, 249502
 Zhang, W., Jahoda, K., Swank, J. H., Morgan, E. H., & Giles, A. B. 1995, *ApJ*, 449, 930